This manuscript has been published online in: Clinical Oral Investigations 2019 Sept
https://doi.org/10.1007/s00784-019-03068-8

Title: Novel non-resorbable polymeric-nanostructured scaffolds for guided bone regeneration.

Authors: Manuel Toledano[1], José L Gutierrez-Pérez[2], Aida Gutierrez-Corrales[2], María A Serrera-Figallo[2], Manuel Toledano-Osorio[1], Juan I Rosales-Leal[1], Mariano Aguilar[3], Raquel Osorio[1*], Daniel Torres-Lagares[2].

Affiliation and adresses:

1. Dental School. University of Granada. Colegio Máximo, Campus de Cartuja s/n. 18017 Granada, Spain. Research Institute IBS.

2. University of Sevilla, Faculty of Dentistry, Oral Surgery Section. Avicena s/n. 41009 Sevilla. Spain.

3. University of Granada, Faculty of Medicine, Biopathology and Medicine Regenerative Institute (IBIMER, CIBM). Avda. de la Investigación 11. 18016 Granada. Spain.

***Corresponding author:**

Prof. Raquel Osorio.

Dental School, University of Granada.

Colegio Máximo, Campus de Cartuja s/n 18017 Granada, Spain.

Phone: +34-958243789; Fax: +34-958240908.

Email: rosorio@ugr.es

Acknowledgements:

Project MAT2017-85999-P MINECO/AEI/FEDER/UE supported by the Ministry of Economy and Competitiveness and European Regional Development Fund. The authors thank the technical support of Álvaro Carrasco-Carmona for the manuscript edition.

Novel non-resorbable polymeric-nanostructured scaffolds for guided bone regeneration.

Abstract

Objective The aim of this study was to evaluate the bone-regeneration efficiency of novel polymeric nanostructured membranes and the effect of zinc, calcium, titanium and bone morpho-protein loading on membranes, through an *in vivo* rabbit model.

Material and Methods Nanostructured membranes of methylmethacrylate were loaded with zinc, calcium, TiO_2 nanoparticles and bone-morphogenetic protein (BMP). These membranes covered the bone defects prepared on the skulls of six rabbits. Animals were sacrificed six weeks after surgery. Micro computed tomography was used to evaluate bone architecture through *BoneJ* pluging and *ImageJ* script. Three histological processing of samples, including von Kossa silver nitrate, toluidine blue and fluorescence by the deposition of calcein were utilized.

Results Zn-Membranes (Zn-Ms) promoted the highest amount of new bone and higher bone perimeter than both unloaded and Ti-Membranes (Ti-Ms). Ca-Membranes (Ca-Ms) attained higher osteoid perimeter and bone perimeter than Zn-Ms. The skeleton analysis showed that Zn-Ms produced more branches and junctions at the trabecular bone than BMP-loaded membranes (BMP-Ms). Samples treated with Ti-Ms showed less bone formation and bony bridging processes. Both Zn-Ms and Ca-Ms achieved higher number of osteoblasts than the control group. BMP-Ms and Ca-Ms originated higher number of blood vessels than Ti-Ms and control group.

Conclusions Zn incorporation in novel nanostructured membranes provided the highest regenerative efficiency for bone healing at the rabbit calvarial defects.

Clinical relevance Zn-Ms promoted osteogenesis and enhanced biological activity, as mineralized and osteoid new bone with multiple interconnected ossified trabeculae appeared in close contact with the membrane.

Key words: non-resorbable polymer, scaffold, bone regeneration, zinc.

Introduction

The basic principle of guided bone regeneration involves the placement of mechanical barriers to protect blood clots and to isolate the bone defect from the surrounding connective tissue, thus providing bone-forming cells with access to a secluded space intended for bone regeneration. This procedure has, in many cases, an unpredictable clinical outcome and remains a challenge [1]. Four stages are used to successfully regenerate bone: *I)* primary closure of the wound to promote undisturbed and uninterrupted healing, *II) angiogenesis* to provide necessary blood supply and undifferentiated *mesenchymal* cells, *III)* space creation and maintenance to facilitate space for bone in-growth and *IV)* stability of the wound to induce blood clot formation and allow uneventful healing. Barrier membranes are used for guided bone regeneration procedures [1, 2].

There are two types of membranes based on the characteristics of resorbability. The use of resorbable tissue-engineered matrices to induce bone formation, when additional support is needed, is not always successful. The main disadvantage of current resorbable membranes is the unpredictable resorption time and the degree of degradation, biocompatibility. The ability to maintain sufficient space to regenerate enough bone for long periods is questioned [1]. Non-resorption might result in shielding of the newly-formed bone from physiological stresses necessary for further remodeling and maturation. Non-resorbable membranes include expanded, high-density and titanium-reinforced polytetrafluoruroethylene, and titanium mesh [1]. Polytetrafluoroethylene (PTFE), a non-resorbable synthetic polymer, still represents the gold standard for clinicians, due to its higher predictability if compared to resorbable membranes. One of the main disadvantages of PTFE are the low adhesiveness for cells and the total absence of the capability of connecting to the bone tissue to providing osseointegration [3]. It is a significant drawback that non-resorbable membranes require of a second surgical intervention to remove the barrier which may injure or compromise the obtained regenerated tissue [1].

Polymethylmethacrylate (PMMA) is a non-resorbable but biocompatible and biostable polymer, which has been widely used to clinically fix prostheses to bone or for vertebroplasty, orthopedic bone cements, skull defect reparation, and mandibular reconstruction, among others [4, 5]. A novel PMMA-based polymeric blend has been designed combining two copolymers, and nanofibers membranes have been prepared by electrospinning. These membranes were shown to be bioactive, biocompatible and resemble bone nanomechanical properties and nanotopography [6].

Functionalization of the polymeric membranes through the incorporation of bioactive components may create a different chemical context, thus enhancing their osteoconductive properties [7]. Improved osteogenic ability [8] and increased osteoconductivity [9] have been associated with the use of calcium- and zinc-containing bioactive materials. Additional use of growth factors such as morphogenetic protein 2 (BMP2) have been recommended [10] and recognized as a potent bone inducer for bone regeneration [11]. TiO_2 nanoparticles might act as primer initiator for the synthesis of a mineral bone matrix, thus perhaps expending the repair and healing of bone defects [12].

Large animal experimental models are important for the development of tissue-engineered constructs. Rabbit is a suitable intermediate model in which bone regeneration studies can be performed [5, 7]. Micro-CT is a promising technique for the observation of microscopic bone structure and both qualification and quantification of bone formation inside and outside of bony defects. It also provides three-dimensional imaging function [13]. Bone histomorphometry represents an essential and sensitive *ex vivo* tool to assess mineralization and cellular activity in the bone [14].

The aim of this study was to examine the regenerative potential of novel nanostructured membranes loaded with zinc, calcium, titanium and bone morphogenetic protein in a non-critical sized calvarial bone defect model of rabbit. The null hypothesis to be tested was that the novel membranes and the bioactive agents do not facilitate bone regeneration.

Materials and methods

Preparation of membranes

Nanostructured membranes were fabricated through electrospinning, with a novel polymeric blend. It is composed of a mixture of two high molecular weight copolymers: methyl methacrylate-co-hydroxyethyl methacrylate (average Mw 200 kDa, PDI<2.5), and methyl acrylate-co-hydroxyethyl acrylate (average Mw 2,000 kDa, PDI<1.5). After electrospinning, the matrix surfaces were reacted with a sodium carbonate buffer solution (333 mM; pH=12.5) for 2 h and gently washed with water. The rest of the technical profiles are described in Osorio et al. [6,15]. Membranes were loaded with calcium, zinc, TiO_2 nanoparticles and human recombinant bone-morphogenetic protein 2, suitable for cell culture with > 95% purity (Sigma Aldrich, Darmstadt, Germany). As the bioactivity of BMP-2 is damaged in the electrospinning process, it was physisorbed onto scaffolds. 1 μg of BMP-2/50μl phosphate buffered saline was dropped in two increments of 25 μl each onto the surface of the scaffold, representing 1 μg of protein

[16]. For zinc and calcium loading, materials underwent continuous shaking in aqueous solutions of $ZnCl_2$ or $CaCl_2$ (containing zinc or calcium at 40 ppm) (pH: 6.5), in order to reach the adsorption equilibrium of metal ions. Then, the suspensions were centrifuged (60 min, 12,000 rpm, two cycles) and the matrices were separated from the supernatant. TiO_2 nanoparticles (20-40 nm) were included in membranes by mixing with the polymers before starting the electrospinning process. A fifth group of unloaded membranes (OH-Ms) was also tested.

Animal experimentation specimens

Six white, New Zealand-breed experimentation rabbits with identical characteristics (age: 6 months; weight: 3.5–4 kg) were selected for the study. Animals were adequately housed; food and water were provided daily *ad libitum* with rabbit-maintenance Harlan-Teckland Lab Animal Diets (2030). The experiment was developed in accordance with the guidelines of the US National Institute of Health (NIH for Care and Use of Laboratory Animals) and European Directive 86/609/EEC regarding the care and use of animals for experimentation. The study also complied with the European Directive 2010/63/EU about the protection of animals used for scientific purposes and with all local laws and regulations. The researchers obtained the approval of the Ethics Committee of the Institution (CCMI-Ref 028/16). As required by the legislative framework, the minimum number of animals was used for ethical reasons. Comparable models have been published concerning the histological and animal experimentation methods [7].

Surgical procedure

Before starting the surgical procedure, vital signs were taken and then immobilisation of the rabbits was carried out. Midazolam (0.25 mg/kg) and propofol (5 mg/kg) were infiltrated intravenously as anaesthetics for induction and an inhalation of 2.8% inspired sevoflurane gas was also used. Analgesia was provided with ketorolac (1.5 mg/kg) and tramadol (3 mg/kg). When the animals were sedated and ready, with a No. 15 scalpel blade incisions were made between the bases of their ears and between their eyes. A surgical triangular field was done after connecting the two incisions with another one in the skull midline. With a Prichard periosteotome, the epithelial, connective, and muscular tissues were separated from the operation field and the skull surface was washed with a sterile saline solution. Six non-critical bone defects (diameter: 6 mm; depth: 3 mm) were created on the parietal bone, on each side of the skull midline, 3 mm

apart, using a trephine (Helmut-Zepf Medical Gmbh, Seitingen, Germany) mounted on an implant micromotor operating at 2000 rpm under saline irrigation. The trephine had an external diameter of 6 mm, a length of 30 mm, and teeth of 2.35 mm. Piezosurgery was used to remove the inner table and the medullary bone in every defect. The depth was controlled with a periodontal probe. A randomly assigned membrane was used to cover each of the five bone defects. The sixth bone defect was left uncovered (unloaded). The randomisation sequence was generated using specific software (Research Randomizer, V. 4.0, Urbaniak GC & Plous S, 2013). The membranes were fixed with the fibrin tissue adhesive Tissucol (Baxter, Hyland S.A. Immuno, Rochester, MI, USA), which was placed on the bone rims adjacent to the defects. Proper adhesion and limited mobility of the membranes were confirmed when the flaps were moved back to their initial positions. Sutures were made on the following planes using resorbable material: periosteal (4/0), sub-epidermal (4/0) and skin (2/0). Simple stitches were used as close as possible to the edge. The wound was carefully cleaned with a sterile saline solution. Anti-inflammatory analgesia (buprenorphine 0.05 mg/kg and carprofen 1 mL/12.5 kg) was administered. The animals were sacrificed six weeks after surgery using an intravenous overdose of potassium chloride solution. The tissue samples were cut and marked individually [7].

Micro computed tomography

After the brain mass was separated and the skull was washed with a sterile saline solution, rabbit skulls were analyzed by Computerized Tomography (Micro-CT) using a Bruker Albira preclinical CT scanner. Acquisitions were performed at the highest quality available; 1000 image 360º radiographic projection at 45 kV, and a 30 minute acquisition time. Tomographic reconstructions were performed using Albira Suite software and standard reconstruction settings [17] generating 2D and 3D volumes with 8.3 voxels/mm resolution. Average bone density in Houndsfield Units (HU) was evaluated using PMOD software (PMOD technologies LLC), positioning 2 mm spherical volumes of interest (VOIs) in a rosette arrangement within each lesion. High resolution reconstructions of a 10 mm^3 volume within each lesion were made using *Albira Suite* software, generating volumes with a 20 voxels/mm resolution. Bone architecture was evaluated using *BoneJ* [18], a free plugin for *ImageJ* [19]. An *ImageJ* script was created to automatically perform the analysis on all subvolumes using the same HU density threshold and *BoneJ* settings using crop (total defect) and crop 150 (central defect) analysis system.

Histological Processing of Samples

Samples were obtained from the skull of each rabbit, cutting them in an anatomical sagittal plane and undecalcified bone were fixed in a 5% buffered formaldehyde solution (pH 7.4). Blocks were retrieved from the regenerated bone defect using an oscillating autopsy saw (Exakt, Kulzer, Wehrheim, Germany). The dissected specimens were immediately immersed in a solution of 4% formaldehyde and 1% calcium embedded in acrylic resin and processed for ground sectioning. The von Kossa (VK) silver nitrate stain (Sigma–Aldrich Chemical Co., Poole, UKwas applied to visualise the mineralised bone (scale bar, 850 µm). VK morphometric study of the bone was carried out by means of an Olympus SZ-CTV stereomicroscope (Olympus, Tokyo, Japan) with 1.2X lenses. Pictures were taken using a digital signal processor (DSP) 5050Zoom camera (Olympus, Tokyo, Japan). One image was taken from each bone defect. The following data were compiled: bone surface (BS), percentage of bone area [BS/total surface (TS)], osteoid surface (OS), percentage of osteoid surface (OS/TS) and bone perimeter (BPm), and bone thickness (BTh). For histological staining and rapid contrast tissue analysis (Merck Toluidine Blue-Merck, Darmstadt, Germany), a metachromatic dye was used. A 1% toluidine blue (TB) solution with a pH of 3.6 was chosen and adjusted with HCl. The samples were exposed to the dye for 10 minutes at room temperature (23.0 $\pm$ 1.0 ºC) with distilled water, and air-dried. Fluorescence images were also obtained to observe the deposition of calcein into the newly deposited bone matrix (scale bar, 500 µm). The toluidine and fluorescence morphometric studies of the bone were carried out by means of an Eclipse LV100 microscope (Nikon, Tokyo, Japan) with 20X and 5X lenses, respectively. Pictures were taken using a DSP DS-Fi1 camera (Nikon, Tokyo, Japan) together with NIS-Elements BR 4.0 software (Nikon, Tokyo, Japan). Osteocytes, osteoblasts and blood vessels were analysed at TB images (scale bars, 50 and 100 µm); four images were taken and analysed in each bone defect. At fluorescence, one image was taken for defect and total surface (TS), osteoid area (OA), the percentage of the total area occupied by osteoid (OA/TS), perimeter of the osteoid (OP), the area occupied by mineralized bone (BA), its percentage respect to the total area of the defect (BA/TS), as well as its perimeter (BP) were recorded. The software *ImageJ* was employed for images analyses.

Statistical Analysis

Means and standard deviations (SD) were obtained. Non-parametrical Friedman tests were employed for variance analysis and multiple post-hoc comparisons were performed. Level of significance was set at $p \leq 0.05$. Analysis was undertaken by means of IBM SPSS Statistics v.20 software package.

Results

Representative 3D Micro-CT images of calvarial defect after treating with the different biomaterials are shown to observe the structures of interest (Fig 1SI). Representative 2D Micro-CT images from each group are observed in Fig 1. Micro computed tomography assessment of both the whole defect (crop) and the centre of the defect (crop 150) was able to distinguish differences ($p<0.05$) among some effects of biomaterials. Crop analysis showed that Zn-Ms produced higher isosurface or bone surface (BS) than the control group (Figs 1a, 1b) (Table 1A SI). The skeleton analysis also visualized higher number of branches and junctions of the trabecular formed bone, when Zn-Ms were used (Figs 1c, 1d) and compared with the control group and with samples treated with BMP-Ms (Figs 1g, 1h) (Table 1A SI). On the other hand, BMP-Ms attained significant higher maximum branch length (Max), than the unloaded membranes (Figs 1k, 1l) (Table 1A SI). When Micro-CT analysis was performed at the centre of the defect (crop 150), Euler characteristics and the spatial connectivity of bone were higher in samples treated with Zn-Ms and BMP-Ms, when compared with the control group (Table 1B SI). The skeleton analysis by Micro-CT also permitted to visualize higher nodes and branch points when Zn-Ms and BMP-Ms were used in comparison to the control group (Figs 1d, 1h). Specimens treated with Zn-Ms achieved longer length of branch than Ca-Ms (Fig 1e, 1f) (Table 1B SI).

The Von Kossa (VK) stain permitted to observe that all bone defects treated with membranes attained higher bone surface (BS) and bone thickness (BTh) than the control group (Tables 1A, 1B). Zn-Ms (Fig 2a) produced the highest amount of new bone (ratio BS/TS), among groups. Zn-Ms also showed higher BTh (Fig 2d) than the unloaded membranes, and produced more osteoid surface (OS) (Fig 2e) than the control group (Tables 1A, 1B). The ratio OS/TS, which expresses the percentage of osteoid respect to the total surface, was similar in all groups. Zn-Ms achieved higher bone perimeter (BPm) (Fig 2c) than those produced by both OH-Ms and Ti-Ms (Table 1B). Intersticial connective tissue was visible in samples treated with Zn-Ms. Adipocyte-like surrounding tissues were also shown in the rest of the groups, especially in the control group. The bone defect in the control group was found to be filled with connective tissue and a few immature bone trabeculae (Fig 3a). Areas of trabecular bone formation could also be identified in the

defects treated with either type of the membrane (Figs. 2b, 3b, 3c, 3d, 3e). Bony bridging processes were observed in all groups, except after using Ti-Ms (Fig 3d).

At the histological images of toluidine blue (TB), the newly-formed bone abutting the membranes showed viable bone and large osteocytes lacunae bridging up the greatest part of both Ca-Ms (Fig 4) and Zn-Ms (Fig 5a). Ca-Ms clearly promoted fusiform cells, osteoid formation and angiogenesis. Zn-Ms created actively new bone beneath the membrane and outside the membrane. At both sides of this membrane, few isles of newly formed bone with osteoblast seam and osteoid were observed, strongly extending from the boundaries of the defect. No signs of inflammation infiltrate could be observed (Fig 5a). The counting of osteocytes was similar among groups (Tables 2A, 2B). Both Zn-Ms and Ca-Ms (Figs 4, 5b) promoted higher number of osteoblasts than the control group. The number of osteoblasts was higher in subjects treated with Zn-loaded than with unloaded membranes (Table 2B). In some fields of all samples, osteoblasts were observed in the process of apposing bone directly on the membrane surface (Fig 5a, 5b). BMP-Ms and Ca-Ms did not produce greater number of osteoblasts than the rest of the membranes but originated higher number of blood vessels than Ti-Ms and the control group (Table 2B). Ca-Ms showed dense and neat collagen fibres, with multiple fusiform cells, that run parallel to the bone defect and the membrane (Fig 5c). A clear fat tissue, lymphocytes and mononuclear inflammatory cells were observed after using Ti-Ms (Fig 5d). The control group promoted less angiogenesis than Ca-Ms, BMP-Ms and Ti-Ms. Similarly, all membranes produced higher vascularization than Ti-Ms (Table 2B). Many large vessels could be detected in samples treated with Zn-Ms and Ca-Ms (Figs 5a, 5b). Small blood vessels were shown in close proximity to the new bone and the Ca-loaded biomaterials (Fig 5c). Images obtained with TB also permitted to observe that apart from Zn-Ms and Ca-Ms, Ti-Ms promoted the formation of bone matrix (Fig 5a, 5b, 5d) over the membrane, outside the surgical defect. No inflammatory cells or multinuclear giant cells were present at the interface with bone in animals treated with Zn-Ms (Fig 5a). Lymphocytes and mononuclear cells over the membrane (Fig 5d) were seen as sight of local inflammation when Ti-Ms were used.

At the histological images obtained with fluorescence calcein, samples treated with unloaded membranes attained higher bone area (BA) than the control group (Tables 3A, 3B) (Figs 6a, 6b). Ca-Ms promoted higher osteoid perimeter (OP) and bone perimeter (BP) than Zn-loaded biomaterials (Tables 3A, 3B) (Figs 6c, 6d).

Discussion

In this experimental research, bone regeneration accounted in all groups, *i.e*, by the end of the study the size of the defects was smaller than its original size (Fig 1 SI). Zn-Ms regenerated significantly more bone within the defect than the other groups and attained higher new formed bone (BS/TS) in comparison to the rest of the groups (Tables 1A, 1B). Therefore, the null hypothesis must be rejected. The increase in structural indexes that was observed after Zn-Ms application (Table 1B) resulted in the replacement of older, overly mature bone with younger and more resilient bone [20]. Osteoid or bone matrix that will be, but not yet, mineralized [21] showed higher surface than in the control group when Zn-Ms were used, a sign of young bone formation [22]. The pattern of the tissue appeared composed by Zn-Ms in close contact with the newly-formed bone and with osteoid (Figs 2e, 5a). Osteoid is secreted by osteoblasts, which initiate its sequential mineralization [23]. The significantly increase of bone surface (BS), *i.e*, mineralized bone matrix excluding osteoid [21] and bone thickness (BTh) became associated with a generalized rise of osteoblasts promoted by all membranes when compared with the control group, especially when Zn-Ms were used (Tables 1, 2). Osteoblasts are induced as a priority at the early healing stage [24].

New bone, associated to multiple interconnected ossified trabeculae (Figs 1d, 2a), was observed directly in contact with the Zn-M surfaces in the regions displaying successful bone conduction [25] (Fig 5a). Newly formed bone was continuous in some scan sections (Figs 1c, 1d) from the defect margin without any invasion of the soft tissue, forming bony bridging images (Figs 1c, 5a). In contrast, defects with no membranes (control group) showed higher blind osteons or end-points than samples treated with Zn-Ms (Table 1B SI). The changing osteonal morphology is likely related to maturation and maintenance of bone vasculature, which is a clear sign of remodeling, based on both nutrient supply and cell recruitment [23]. Osteogenesis is always preceded by angiogenesis [13]. Thereby, it is reasonably to suggest that incorporation of Zn provides higher regenerative efficiency for bone healing.

Not only osteogenesis but enhanced biological activity was determined attending to the amount of osteoblasts when Zn-Ms and Ca-Ms were used (Table 2B). Polymer-based scaffold/membranes loaded with Zn have previously been shown to enhance cell proliferation/wound healing [26]. Zinc ion has also been recognized as a promising osteoimmunomodulator with actions on macrophage polarization and osteogenic cells differentiation [27]. Formation of new bone indicates that membranes can induce osteoblasts growth and differentiation to fill, or partially fill intracortical pores by nucleating clusters. These former mineral deposits induce their subsequent fusion to produce amorphous calcium phosphate and ultimately apatite

crystals [28], thus reactivating bone-lining cells to bone-forming osteoblasts. Moreover, the pore connectivity described in these membranes [6] might influence the possibility that a greater number of osteoblasts can penetrate the porous structure [29]. In addition, an ingrowth of micro vessels was also found nearby the membrane when Zn-Ms were used (Fig 5a), contributing to the integration of the biomaterial in the tissue [30]. Following vessel extension, bone regeneration occurred alongside the newly formed vessels [13]. Furthermore, Zn has been demonstrated to protect both collagen from degradation and the seed crystallite sparce collagen for re-mineralization. Zn also influences signaling pathway and stimulates the metabolic effect for hard tissue mineralization [31].

When Ca-Ms were used, discontinuous bony regeneration was observed parallel to the membrane, trying to bridge both sides of the defect (Figs 1f, 3b). Small trabeculae were obtained after using Ca-Ms in comparison to those achieved by Zn-Ms, as bone perimeter (BP) and osteoid perimeter (OP) measurements showed significant higher values when Ca-Ms were used (Table 3B) (Figs 6c, 6d). This complied with the maximum branch length obtained at the center of the defect after using Ca-Ms (Table 1B SI). Ca-Ms did not exhibit the osteogenic potential that expected (Table 1B). The scarce angiogenesis that was observed, in comparison with that obtained by the other groups, played a crucial role in bone neogenesis and in all regenerative processes because sufficient nutritional support is essential [30]. Fibrous connective tissue, which prevents osteogenesis entirely or partially [32], was observed at the base of the Ca-Ms (Fig 5b). It is hypothesized that cells cannot perform matrix calcification due to the lack of bone-derived growth and differentiation factors in bone defects [33].

Bone islands appeared not only at the margins of the defect, but scattered throughout the whole defect when BMP-Ms were used (Fig 3c). These findings became associated to higher maximum branch length and connectivity (Fig 1g) than those observed in specimens treated with unloaded membranes or control group, respectively (Table 1A SI). Slight radiopacity (Fig 1h) was also observed, and corresponded with lower new bone (BS/TS) than that attained by the Zn-Ms (Table 2B). Contrary to what it has been previously found [25], BMP-Ms did not induce significant osteoblasts differentiation when compared with the rest of the study groups (Table 2B). Probably, the use of these porcine-derived collagen resorbable membranes combined with rhBMP9 used by Fujioka-Kobayashi et al. [25] make comparison difficult respect to the BMP-PMMA/loaded membranes employed in the present study. The influence of the carrier system on the effective delivery of BMP on bone formation [25] poses a point to research on in future strategies.

Commonly, bone regenerated under stable conditions that are free from pressure and tension. Therefore, more regeneration should occur around the defect margin and less in the central region. A stiffer biomaterial, as Ti-Ms, would provide a more protected environment and more bone regeneration [5]. The bone tissues at the defect showed scarce regeneration within the region of interest, limited to the margins, where minor new bone formation was shown (Figs 1i, 3d). This data concurred with the lowest bone surface (BS) and bone perimeter (BPm) that Ti-loaded membranes attained among groups (Table 1A). However, formation of bone matrix [21] could be adverted, besides, over the membrane, outside the defect (Fig 5d). Ti-particle induced inhibition on osteogenic activity of mesenchymal-stem cells and hindered the expression of multiple signaling pathway compounds. As a result, Ti-particles inhibited bone formation [34]. The defect was also characterized by infiltration of fat tissue and lower vascularization, though several blood vessels were observed in the preset sample (Fig 5d). Insufficient bone vascularity results in decreased bone formation [13] and complied with the presence of lymphocytes, mononucleated cells, and a relatively low number of osteoblasts (Table 2A) (Fig 5d). Fibroblast bands near a scaffold may attract lymphocytes and allow for infiltration of inflammatory factors, thereby restricting osteoblast proliferation and differentiation and consequently inhibiting new bone formation close to the membrane [35].

When the unloaded membranes were used, bone regeneration was observed throughout both the center and the edges of the defects, but bone formation occurred mainly from the periphery of the defect, leaving the center of the defect almost empty (Figs 1k, 1l, 3e). No significant bone formation and consolidation of the untreated defect was achieved and observed through histological and Micro-CT analysis. In the control group, bone regenerated only at the edge of the defect (Fig 3a), without evidence of bringing, and there was reduction in the defect area. The bone area (BA) was the smallest among groups but significantly different from samples treated with unloaded membranes (Table 3B) (Figs 6a, 6b). Some osteocytes, osteoblasts and blood vessels were observed at the defects, though areas of fibrous tissue nearby the trabeculae bone (Figs 1a, 1b) were also present, as it was reported by Oktay et al. [36]. At the end of the study, the defect was almost completely occupied with fibrous or adipose-like characteristic of immature tissue [7] and quite a few newly-formed, island-like bone (Fig 1b), as it was also found by Park et al. [37]. These islands could be the product of osteogenic activity from the surrounding periostium and dura mater [7]. Nevertheless, an almost occluded defect was also seen at some histological sections. Negatively charged carboxylated surfaces have been shown to produce smooth inflammatory reactions after

polymers implantation, diminishing macrophage-mediated inflammatory activity and promoting regulatory T cell phenotypes. This results in low thickness or no fibrotic capsule formation around the tissues [38].

It should be taken into account that these novel membranes are fiber scaffolds. They may have promoted tissue integration by mimicking the architecture and the nanomechanical properties of the natural extracellular bone matrix [6]. Substrate stiffness and nanotopography have been reported to have a crucial effect on cell behavior and tissue integration [39, 40]. Immune cells are also sensitive to the microstructural and textural properties of materials. It seems that surface topography also plays an important role in stimulating the production of pro-inflammatory cytokines by macrophages which, in turn, regulates osteogenic or degradative processes around implanted biomaterials [41]. Further research is needed in these fields.

The relatively small sample size is a limitation of the present research. More studies are required to understand the new bone formation patterns at different time points. Within the limits of the present investigation, the histological and histomorphometric analysis of the regenerated tissues might provide useful information regarding the nature and amount of newly formed bone of the five tested biomaterials. Zn-Ms were in close contact with newly formed bone and showed the same pattern of bone formation surrounding the membrane producing a bridge-like network between areas of new bone. A main strength of our study is that Zn-Ms in fact acts as bioactive modulator for signals communicated to the underlying defect. These results provide evidence that Zn-Ms may be useful for tissue engineering, but should be taken with caution until they are directly corroborated in human maxillary and mandible bone locations.

Conclusions

Novel non-resorbable PMMA-based and nanostructured membranes may be useful for guided bone regeneration. Zn incorporation in novel membranes provided the highest regenerative efficiency for bone healing at the rabbit calvarial defects. Zn-Ms promoted osteogenesis and enhanced biological activity, as mineralized and osteoid new bone with multiple interconnected ossified trabeculae, but without soft tissue invasion, appeared in close contact with the membrane.

Compliance with ethical standards

Declaration of interest: None

Funding: Project MAT2017-85999-P MINECO/AEI/FEDER/UE supported by the Ministry of Economy and Competitiveness (MINECO) and European Regional Development Fund (FEDER).

Ethical Approval: The experiment was developed in accordance with the guidelines of the US National Institute of Health (NIH for Care and Use of Laboratory Animals) and European Directive 86/609/EEC regarding the care and use of animals for experimentation. The study also complied with the European Directive 2010/63/EU about the protection of animals used for scientific purposes and with all local laws and regulations. Animals were adequately housed; food and water were provided daily *ad libitum* with rabbit-maintenance Harlan-Teckland Lab Animal Diets (2030). The researchers obtained the approval of the Ethics Committee of the Institution (CCMI-Ref 028/16).

Data availability statement: The raw/processed data required to reproduce these findings cannot be shared at this time as the data also forms part of an ongoing study.

References

1. Zhang F, Zhang WB, Shi Z, Wang D, Jin J, Jiang L (2013) Nanowire-haired inorganic membranes with superhydrophilicity and underwater ultralow adhesive superoleophobicity for high-efficiency oil/water separation. Adv Mater Deerfield Beach Fla 25:4192–4198. https://doi.org/10.1002/adma.201301480
2. Omar O, Elgali I, Dahlin C, Thomsen P (2019) Barrier membranes: more than the barrier effect? J Clin Periodontol. https://doi.org/10.1111/jcpe.13068
3. Sam G, Pillai BRM (2014) Evolution of Barrier Membranes in Periodontal Regeneration-"Are the third Generation Membranes really here?". J Clin Diagn Res JCDR 8:ZE14–ZE17. https://doi.org/10.7860/JCDR/2014/9957.5272
4. Punet X, Mauchauffé R, Rodríguez-Cabello JC, Alonso M, Engel E, Mateos-Timoneda MA (2015) Biomolecular functionalization for enhanced cell-material interactions of poly(methyl methacrylate) surfaces. Regen Biomater 2:167–175. https://doi.org/10.1093/rb/rbv014
5. Kim S, Hwang Y, Kashif M, Jeong D, Kim G (2016) Evaluation of Bone Regeneration on Polyhydroxyethyl-polymethyl Methacrylate Membrane in a Rabbit Calvarial Defect Model. Vivo Athens Greece 30:587–591
6. Osorio R, Alfonso-Rodríguez CA, Osorio E, Medina-Castillo AL, Alaminos M, Toledano-Osorio M, Toledano M (2017) Novel potential scaffold for periodontal tissue engineering. Clin Oral Investig 21:2695–2707. https://doi.org/10.1007/s00784-017-2072-8
7. Castillo-Dalí G, Castillo-Oyagüe R, Terriza A, Saffar JL, Batista-Cruzado A, Lynch CD, Sloan AJ, Gutiérrez-Pérez JL, Torres-Lagares D (2016) "Pre-prosthetic use of poly(lactic-co-glycolic acid) membranes treated with oxygen plasma and TiO2 nanocomposite particles for guided bone regeneration processes." J Dent 47:71–79. https://doi.org/10.1016/j.jdent.2016.01.015
8. Nandakumar A, Yang L, Habibovic P, van Blitterswijk C (2010) Calcium phosphate coated electrospun fiber matrices as scaffolds for bone tissue engineering. Langmuir ACS J Surf Colloids 26:7380–7387. https://doi.org/10.1021/la904406b
9. Seol Y-J, Kim K-H, Kang YM, Kim IA, Rhee S-H (2009) Bioactivity, pre-osteoblastic cell responses, and osteoconductivity evaluations of the electrospun non-woven SiO2-CaO gel fabrics. J Biomed Mater Res B Appl Biomater 90:679–687. https://doi.org/10.1002/jbm.b.31334

10. Jovanovic SA, Hunt DR, Bernard GW, Spiekermann H, Wozney JM, Wikesjö UME (2007) Bone reconstruction following implantation of rhBMP-2 and guided bone regeneration in canine alveolar ridge defects. Clin Oral Implants Res 18:224–230. https://doi.org/10.1111/j.1600-0501.2006.01324.x

11. Saulacic N, Fujioka-Kobayashi M, Kobayashi E, Schaller B, Miron RJ (2017) Guided bone regeneration with recombinant human bone morphogenetic protein 9 loaded on either deproteinized bovine bone mineral or a collagen barrier membrane. Clin Implant Dent Relat Res 19:600–607. https://doi.org/10.1111/cid.12491

12. Sun Z, Kim JH, Zhao Y, Attard D, Dou SX (2013) Morphology-controllable 1D–3D nanostructured TiO2 bilayer photoanodes for dye-sensitized solar cells. Chem Commun 49:966–968. https://doi.org/10.1039/C2CC37212F

13. Udagawa A, Sato S, Hasuike A, Kishida M, Arai Y, Ito K (2013) Micro-CT observation of angiogenesis in bone regeneration. Clin Oral Implants Res 24:787–792. https://doi.org/10.1111/j.1600-0501.2012.02458.x

14. Erben RG, Jolette J, Chouinard L, Boyce R (2017) Application of Histopathology and Bone Histomorphometry for Understanding Test Article-Related Bone Changes and Assessing Potential Bone Liabilities. In: Bone Toxicology. Springer, pp 253–278

15. Osorio R, Alfonso-Rodríguez CA, Medina-Castillo AL, Alaminos M, Toledano M (2016) Bioactive Polymeric Nanoparticles for Periodontal Therapy. PloS One 11:e0166217. https://doi.org/10.1371/journal.pone.0166217

16. Suliman S, Xing Z, Wu X, Xue Y, Pedersen TO, Sun Y, Døskeland AP, Nickel J, Waag T, Lygre H, Finne-Wistrand A, Steinmüller-Nethl D, Krueger A, Mustafa K (2015) Release and bioactivity of bone morphogenetic protein-2 are affected by scaffold binding techniques in vitro and in vivo. J Controlled Release 197:148–157. https://doi.org/10.1016/j.jconrel.2014.11.003

17. Sánchez F, Orero A, Soriano A, Correcher C, Conde P, González A, Hernández L, Moliner L, Rodríguez-Alvarez MJ, Vidal LF, Benlloch JM, Chapman SE, Leevy WM (2013) ALBIRA: a small animal PET⁄SPECT⁄CT imaging system. Med Phys 40:051906. https://doi.org/10.1118/1.4800798

18. Doube M, Kłosowski MM, Arganda-Carreras I, Cordelières FP, Dougherty RP, Jackson JS, Schmid B, Hutchinson JR, Shefelbine SJ (2010) BoneJ: Free and extensible bone image analysis in ImageJ. Bone 47:1076–1079. https://doi.org/10.1016/j.bone.2010.08.023

19. Schneider CA, Rasband WS, Eliceiri KW (2012) NIH Image to ImageJ: 25 years of image analysis. Nat Methods 9:671–675

20. Rubin MR, Zhou H, Cusano NE, Majeed R, Omeragic B, Gomez M, Nickolas TL, Dempster DW, Bilezikian JP (2018) The Effects of Long-term Administration of rhPTH(1-84) in Hypoparathyroidism by Bone Histomorphometry. J Bone Miner Res 33:1931–1939. https://doi.org/10.1002/jbmr.3543

21. Parfitt AM, Drezner MK, Glorieux FH, Kanis JA, Malluche H, Meunier PJ, Ott SM, Recker RR (1987) Bone histomorphometry: standardization of nomenclature, symbols, and units. Report of the ASBMR Histomorphometry Nomenclature Committee. J Bone Miner Res Off J Am Soc Bone Miner Res 2:595–610. https://doi.org/10.1002/jbmr.5650020617

22. La Monaca G, Iezzi G, Cristalli MP, Pranno N, Sfasciotti GL, Vozza I (2018) Comparative Histological and Histomorphometric Results of Six Biomaterials Used in Two-Stage Maxillary Sinus Augmentation Model after 6-Month Healing. BioMed Res Int 2018:9430989. https://doi.org/10.1155/2018/9430989

23. Maggiano IS, Maggiano CM, Clement JG, Thomas CDL, Carter Y, Cooper DML (2016) Three-dimensional reconstruction of Haversian systems in human cortical bone using synchrotron radiation-based micro-CT: morphology and quantification of branching and transverse connections across age. J Anat 228:719–732. https://doi.org/10.1111/joa.12430

24. Chang Y-C, Ho K-N, Feng S-W, Huang H-M, Chang C-H, Lin C-T, Teng N-C. Pan YH, Chang W-J (2016) Fibronectin-Grafted Titanium Dental Implants: An In Vivo Study. BioMed Res Int 2016:2414809. https://doi.org/10.1155/2016/2414809

25. Fujioka-Kobayashi M, Kobayashi E, Schaller B, Mottini M, Miron RJ, Saulacic N (2017) Effect of recombinant human bone morphogenic protein 9 (rhBMP9) loaded onto bone grafts versus barrier membranes on new bone formation in a rabbit calvarial defect model. J Biomed Mater Res A 105:2655–2661. https://doi.org/10.1002/jbm.a.36125

26. Augustine R, Malik HN, Singhal DK, Mukherjee A, Malakar D, Kalarikkal N, Thomas S (2014) Electrospun polycaprolactone/ZnO nanocomposite membranes as biomaterials with antibacterial and cell adhesion properties. J Polym Res 21:347. https://doi.org/10.1007/s10965-013-0347-6

27. Liu W, Li J, Cheng M, Wang Q, Yeung KWK, Chu PK, Zhang X (2018) Zinc- Modified Sulfonated Polyetheretherketone Surface with Immunomodulatory Function for Guiding Cell Fate and Bone Regeneration. Adv Sci 5:1800749. https://doi.org/10.1002/advs.201800749

28. Dey A, Bomans PHH, Müller FA, Will J, Frederik PM, de With G, Sommerdijk NAJM (2010) The role of prenucleation clusters in surface-induced calcium phosphate crystallization. Nat Mater 9:1010–1014. https://doi.org/10.1038/nmat2900

29. Guarnieri R, Belleggia F, DeVillier P, Testarelli L (2018) Histologic and Histomorphometric Analysis of Bone Regeneration with Bovine Grafting Material after 24 Months of Healing. A Case Report. J Funct Biomater 9:E48. https://doi.org/10.3390/jfb9030048

30. Turri A, Dahlin C (2015) Comparative maxillary bone-defect healing by calcium-sulphate or deproteinized bovine bone particles and extra cellular matrix membranes in a guided bone regeneration setting: an experimental study in rabbits. Clin Oral Implants Res 26:501–506. https://doi.org/10.1111/clr.12425

31. Toledano M, Yamauti M, Ruiz-Requena ME, Osorio R (2012) A ZnO-doped adhesive reduced collagen degradation favouring dentine remineralization. J Dent 40:756–765. https://doi.org/10.1016/j.jdent.2012.05.007

32. Tayşi M, Atalay B, Çankaya B, Yıldırım S (2018) Effects of single- and double-layered resorbable membranes and platelet-rich fibrin on bone healing. Clin Oral Investig 22:1689–1695. https://doi.org/10.1007/s00784-017-2259-z

33. Schmitz JP, Schwartz Z, Hollinger JO, Boyan BD (1990) Characterization of rat calvarial nonunion defects. Acta Anat (Basel) 138:185–192

34. Ping Z, Wang Z, Shi J, Wang L, Guo X, Zhou W, Hu X, Wu X, Liu Y, Zhang W, Yang H, Xu Y, Gu Y, Geng D (2017) Inhibitory effects of melatonin on titanium particle-induced inflammatory bone resorption and osteoclastogenesis via suppression of NF-κB signaling. Acta Biomater 62:362–371. https://doi.org/10.1016/j.actbio.2017.08.046

35. Zhang N, Zhao D, Liu N, Wu Y, Yang J, Wang Y, Xie H, Ji Y, Zhou C, Zhuang J, Wang Y, Yan J (2018) Assessment of the degradation rates and effectiveness of different coated Mg-Zn-Ca alloy scaffolds for in vivo repair of critical-size bone defects. J Mater Sci Mater Med 29:138. https://doi.org/10.1007/s10856-018-6145-2

36. Oktay EO, Demiralp B, Demiralp B, Senel S, Cevdet Akman A, Eratalay K, Akincibay H (2010) Effects of platelet-rich plasma and chitosan combination on bone regeneration in experimental rabbit cranial defects. J Oral Implantol 36:175–184. https://doi.org/10.1563/AAID-JOI-D-09-00023

37. Park CK, Lee Y, Kim KH, Lee ZH, Joo M, Kim H-H (2014) Nrf2 is a novel regulator of bone acquisition. Bone 63:36–46. https://doi.org/10.1016/j.bone.2014.01.025

38. Mariani E, Lisignoli G, Borzì RM, Pulsatelli L (2019) Biomaterials: Foreign Bodies or Tuners for the Immune Response? Int J Mol Sci 20:E636. https://doi.org/10.3390/ijms20030636

39. Pinese C, Lin J, Milbreta U, Li M, Wang Y, Leong KW, Chew SY (2018) Sustained delivery of siRNA/mesoporous silica nanoparticle complexes from nanofiber scaffolds for long-term gene silencing. Acta Biomater 76:164–177. https://doi.org/10.1016/j.actbio.2018.05.054

40. Yang Y, Wang K, Gu X, Leong KW (2017) Biophysical Regulation of Cell Behavior—Cross Talk between Substrate Stiffness and Nanotopography. Eng Beijing China 3:36–54. https://doi.org/10.1016/J.ENG.2017.01.014

41. Sadowska JM, Wei F, Guo J, Guillem-Marti J, Ginebra M-P, Xiao Y (2018) Effect of nano-structural properties of biomimetic hydroxyapatite on osteoimmunomodulation. Biomaterials 181:318–332. https://doi.org/10.1016/j.biomaterials.2018.07.058

Figure captions

Fig. 1 Representative peripheral micro-computed tomography (µ-CT) in 2-D dimensions of the bone defect in the control group (**a**, **b**); 2 scan planes (among 200) were selected: a, 96th; b, 175th. Zn-M treated group (**c, d**); 2 scan planes (among 200) were selected: c, 135th; d, 148th. Ca-M treated group (**e, f**); 2 scan planes (among 200) were selected: e, 84th scan plane; f, 150th scan plane. BMP-M treated group (**g, h**); 2 scan planes (among 200) were selected: g, 72th; h, 106th. Ti-M treated group (**i, j);** 2 scan planes (among 200) were selected: i, 114th; j, 131th. Unloaded membrane treated group (**k, l**); 2 scan planes (among 200) were selected: k, 114th; l, 129th. Arrow heads point out the edge defects. Single pointers correspond with soft tissue. Double pointers are membranes. Asterisks (*) are old trabecular bone. Island-like bone formations correspond with faced pointers. Single arrows are new bone. Interconnected ossified trabeculae and branches are signaled by double arrows. Bony bridging formations are identified with faced arrows

Fig. 2 Bone histomorphometry obtained after zinc-loaded membrane, by coloration with von Kossa silver nitrate stain to visualize mineralized bone, at six weeks of follow up. **a**, histology section including the bone defect and the region of interest (ROI), showing a large formation of bone. **b**, total surface (TS) at ROI; asterisks (*) show the presence of interstitial connective tissue. Bony bridging (BB) images are observed. **c**, Binary image of trabecular bone area and Bone perimeter (BPm) at ROI. **d**, Bone thickness (BTh) with the traced measurements at ROI. **e**, Osteoid surface (OS), in yellow, at ROI

Fig. 3 Bone histomorphometry obtained by coloration with von Kossa silver nitrate method to visualize mineralized bone, at six weeks of follow up, after using no membrane- control (**a**), Ca- (**b**), BMP- (**c**), Ti- (**d**), and unloaded membrane (**e**). Trabecular bone formation were observed along the margin of calvarial defect (arrow head), and within the defect. **BB,** Bony bridging; **FT,** fibrous tissue**; Mbr**, membrane; **NB**, new bone; **OB**, old bone. Pointers show scattered bone islands, in correspondence with new bone

Fig. 4 Bone histology obtained after calcium-loaded membrane, by coloration with toluidine blue to visualize mineralized bone, at six weeks of healing time. Segments of trabecular new formed (**NB**) bone are observed. The single arrows indicate osteoblasts seams deposing new osteoid (**Os**). The double arrows indicate the presence of osteocytes. Double pointers indicate fusiform cells. Some blood vessels are identified by asterisks (*). A pronounced infiltration of mononuclear cells (pointers) is observed. Multinuclear giant cells are shown (faced arrows)

Fig. 5 Bone histology obtained after using Zn- (**a**), Ca- (**b, c**) and Ti- (**d**)-loaded membranes by coloration with toluidine blue to visualize mineralized bone, at six weeks of healing time. Single arrows indicate the

presence of osteoblasts; double arrows indicate the presence of osteocytes; faced arrows mean blood vessels; pointers indicate fibrous connective tissue; double pointers indicate osteoclasts; asterisks (*) mean collagen fibers. **BB**, bony bridging; **Fc**, fusiform cells; **FT**, fat tissue; **Lc**, lymphocytes; **Mc**, macrophages; **Mnc**, mononuclear cells; **NB**, trabecular new bone; **Os**, osteoid

Fig. 6 Bone histology obtained by fluorescence with calcein at the region of interest to visualize mineralized bone, at six weeks of healing time in the control group (**a**), after using unloaded-Ms (**b**), Zn-Ms (**c**) and Ca-Ms (**d**). Arrows indicate the osteoid perimeter (**OP**) (partial limit). Pointers indicate bone perimeter (**BP**) (partial limit)

Table 1A: Histomorphometric data obtained within the new bone formed at the region of interest (Mean±SD).

	BS (mm^2)	BS/TS (%)	OS (mm^2)	OS/TS (%)	BPm (mm)	BTh (mm)
Ctr	1.63 ± 0.78	0.28 ± 0.07	0.31 ± 0.30	0.05 ± 0.05	46.09 ± 19.86	0.58 ± 0.22
Zn	3.27 ± 1.15	0.39 ± 0.11	0.48 ± 0.24	0.06 ± 0.02	100.33 ± 18.60	1.64 ± 0.23
Ca	2.70 ± 0.82	0.31 ± 0.07	0.46 ± 0.21	0.05 ± 0.02	82.56 ± 37.69	1.58 ± 0.47
BMP	2.47 ± 0.91	0.28 ± 0.07	0.46 ± 0.30	0.05 ± 0.03	79.31 ± 16.32	1.38 ± 0.24
Ti	2.45 ± 0.66	0.31 ± 0.09	0.44 ± 0.14	0.06 ± 0.03	65.15 ± 18.28	1.28 ± 0.31
Unloaded	2.52 ± 0.67	0.29 ± 0.06	0.46 ± 0.20	0.06 ± 0.03	70.37 ± 7.39	1.14 ± 0.37

Table 1B: Statistical results (*P* values). Bold numbers indicate significance at $P < 0.05$.

	BS	BS/TS	OS	OS/TS	BPm	BTh
Ctr - Zn	**0.04**	**0.04**	**0.03**	0.90	0.41	**0.000**
Ctr - Ca	**0.04**	0.17	0.27	0.80	0.31	**0.007**
Ctr - BMP	**0.01**	0.18	0.45	1.00	0.94	**0.006**
Ctr -Ti	**0.03**	0.7	0.11	0.73	0.76	**0.01**
Ctr - Unloaded	**0.03**	0.23	0.18	0.63	0.37	**0.02**
Zn - Ca	0.27	**0.03**	0.86	0.83	0.12	0.83
Zn- BMP	0.16	**0.07**	0.61	0.93	0.50	0.09
Zn - Ti	0.86	**0.01**	0.51	1.00	**0.01**	0.07
Zn - Unloaded	0.23	**0.04**	0.79	0.87	**0.03**	**0.01**

Abbreviations: BS: Bone Surface; OS: Osteoid Surface; BPm: Bone Perimeter; BTh: Bone Thickness; Ctr: control; Zn: zinc; Ca: calcium; BMP: Bone morphogenetic protein; Ti: titanium.

Table 2A: Bone cells and blood vessels detected within the new bone formed at the region of interest (Mean±SD).

	Osteocytes/mm^2	Osteoblasts/mm^2	Blood Vessels/mm^2
Ctr	2934.74 ± 1231.68	154.97 ± 51.66	11.66 ± 2.95
Zn	3359.91 ± 783.15	312.63 ± 92.41	14.77 ± 1.88
Ca	3200.29 ± 1450.04	307.16 ± 96.23	16.31 ± 3.67
BMP	3888.35 ± 1739.98	314.26 ± 164.03	16.35 ± 4.49
Ti	3053.13 ± 924.84	264.76 ± 81.70	6.04 ± 2.62
Unloaded	2796.25 ± 646.30	247.61 ± 66.36	16.58 ± 10.11

Table 2B: Statistical results (*P* values). Bold numbers indicate significance at $P < 0.05$.

	Osteocytes	Osteoblasts	Blood vessels
Ctr - Zn	0.33	**0.00**	0.28
Ctr - Ca	0.45	**0.02**	**0.03**
Ctr - BMP	0.22	**0.04**	**0.04**
Ctr -Ti	0.55	**0.01**	**0.01**
Ctr - Unloaded	0.61	0.11	0.36
Ti- Ca	0.29	0.36	**0.00**
Ti- Zn	0.52	0.15	**0.00**
Ti- BMP	0.18	0.97	**0.00**
Ti- COOH	0.66	0.59	**0.01**
Zn- Ca	0.78	0.38	0.17
Zn- BMP	0.44	0.15	0.47
Zn- Ti	0.52	**0.03**	**0.00**
Zn-Unloaded	0.24	**0.02**	1.00

Abbreviations: Ctr: control; Zn: zinc; Ca: calcium; BMP: Bone morphogenetic protein; Ti: titanium.

Table 3A: Histomorphometric data obtained by fluorescence with calcein, within the new bone formed at the region of interest (Mean±SD).

	OA (mm^2)	OA/TS (%)	OP (mm)	BA (mm^2)	BA/TS (%)	BP (mm)
Ctr	0.931 ± 0.593	0.405 ± 0.178	57.868 ± 28.779	1.249 ± 0.514	0.595 ± 0.178	60.716 ± 28.283
Zn	1.018 ± 0.608	0.388 ± 0.223	58.453 ± 29.389	1.589 ± 0.753	0.612 ± 0.223	61.893 ± 28.266
Ca	1.060 ± 0.460	0.426 ± 0.195	70.403 ± 26.119	1.555 ± 0.713	0.574 ± 0.195	72.668 ± 25.001
BMP	1.090 ± 0.557	0.418 ± 0.212	71.024 ± 42.264	1.628 ± 0.779	0.582 ± 0.212	72.909 ± 41.767
Ti	1.088 ± 0.751	0.387 ± 0.221	71.544 ± 39.316	1.588 ± 0.719	0.613 ± 0.221	71.069 ± 37.586
Unloaded	1.159 ± 0.897	0.398 ± 0.271	60.472 ± 24.351	1.682 ± 0.797	0.602 ± 0.271	62.489 ± 25.857

Table 3B: Statistical results (*P* values). Bold numbers indicate significance at $p<0.05$.

	OP (mm)	BA (mm^2)	BP (mm)
Ctr-Unloaded	0.50	**0.01**	0.52
Ca-Zn	**0.03**	0.86	**0.03**

Abbreviations: TS: Total Surface; OA: Osteoid Area; OP: Osteoid Perimeter; BA: Bone Area; BP: Bone Perimeter; Ctr: control; Zn: zinc; Ca: calcium; BMP: Bone morphogenetic protein; Ti: titanium.

Figure 1

Click here to access/download;Figure;Figure 1.tif

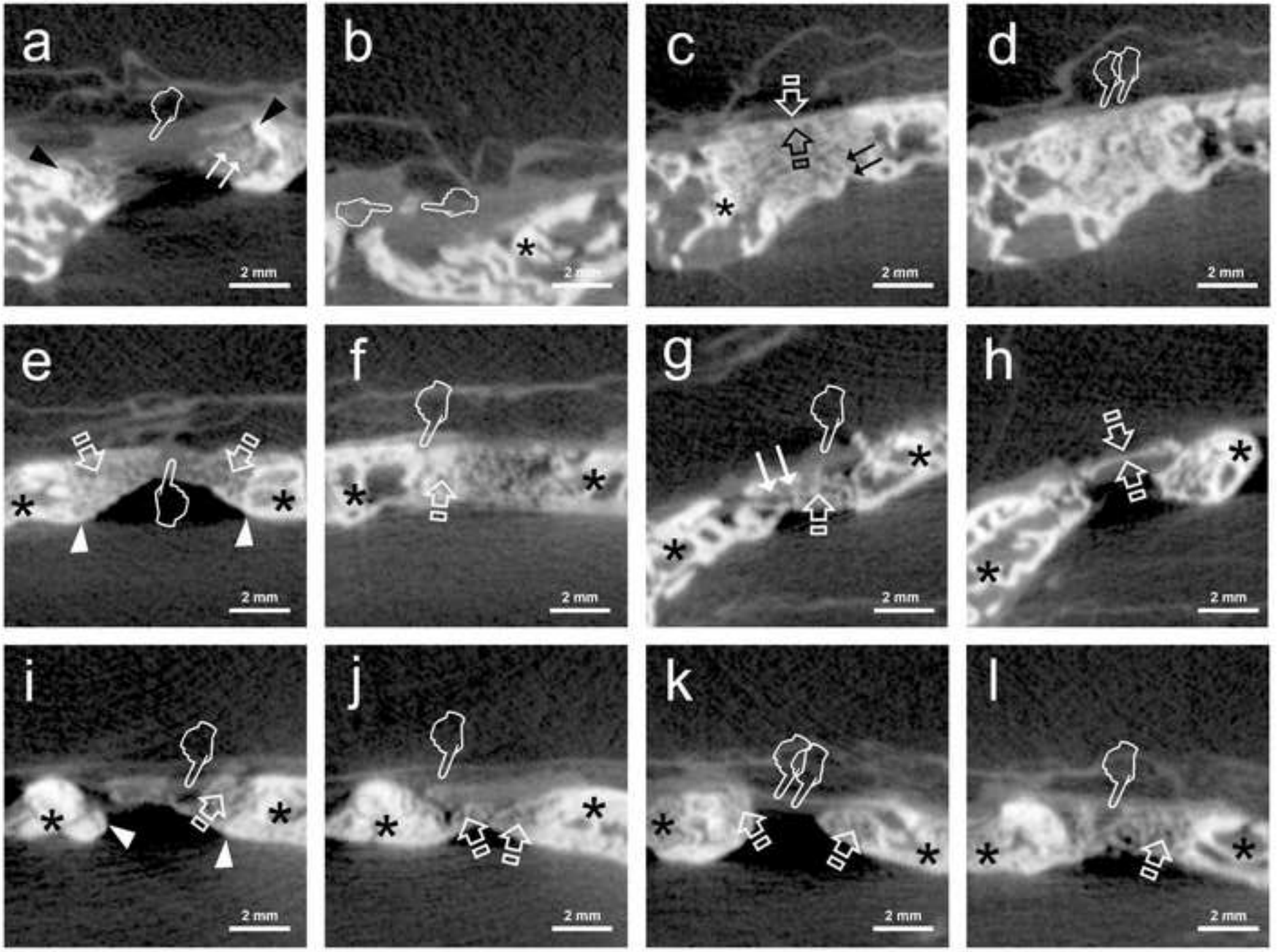

Figure 2

Click here to access/download;Figure;Figure 2.tif

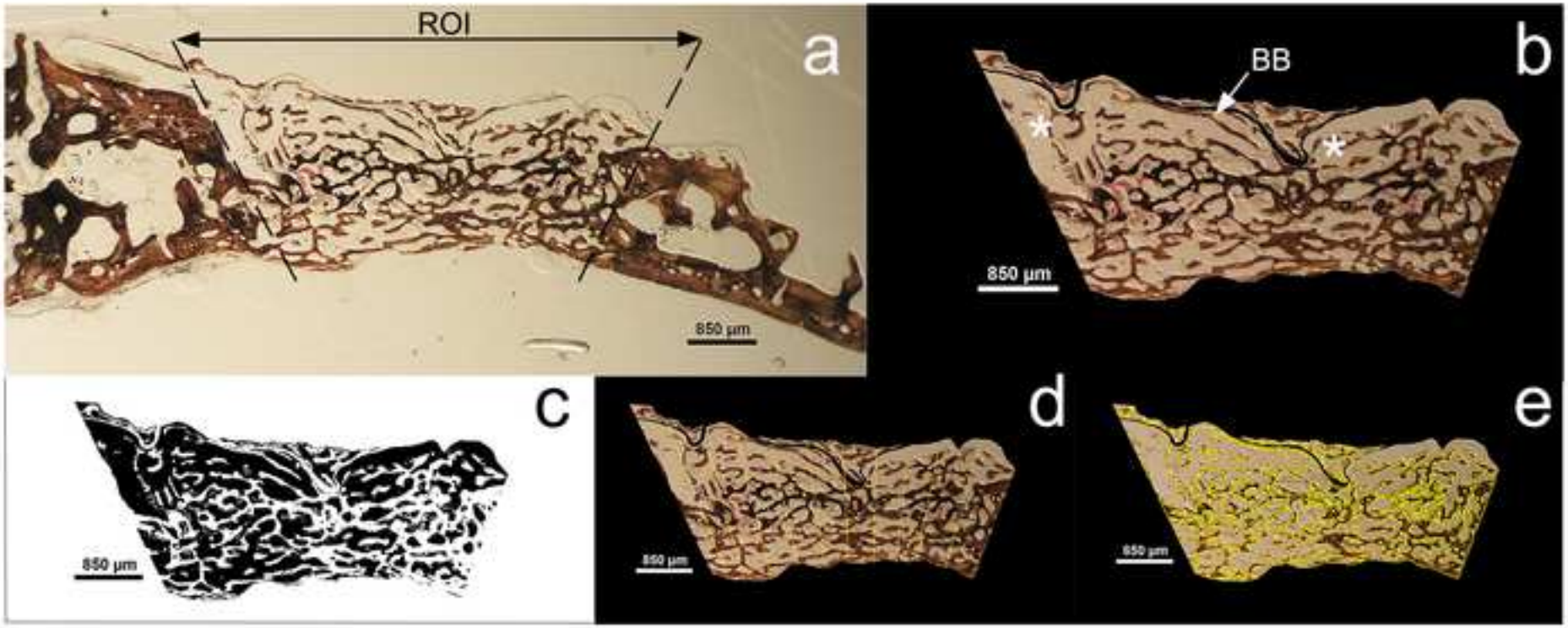

Figure 3

Click here to access/download;Figure;Figure 3.tif

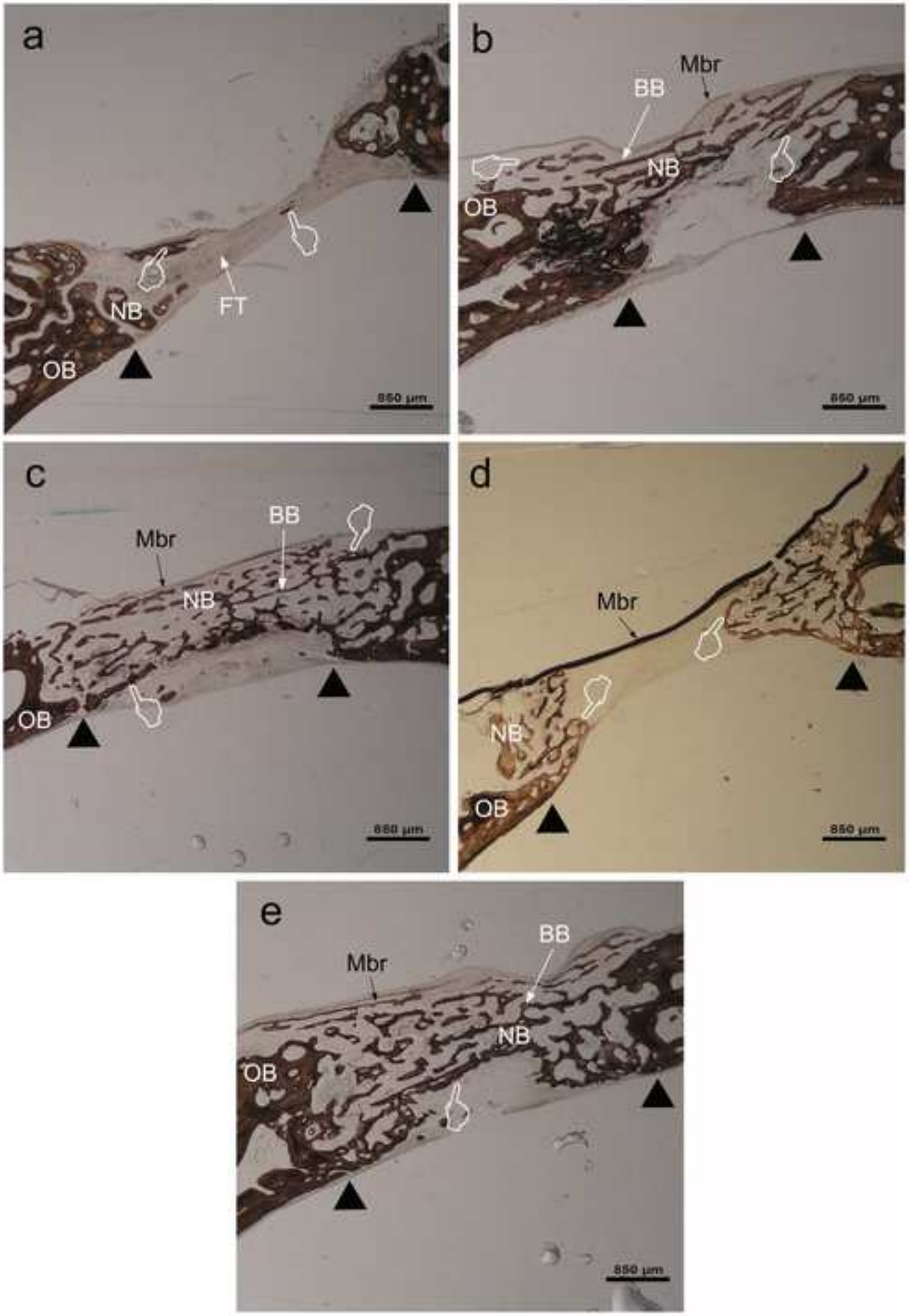

Figure 4

Click here to access/download;Figure;Figure 4.tif

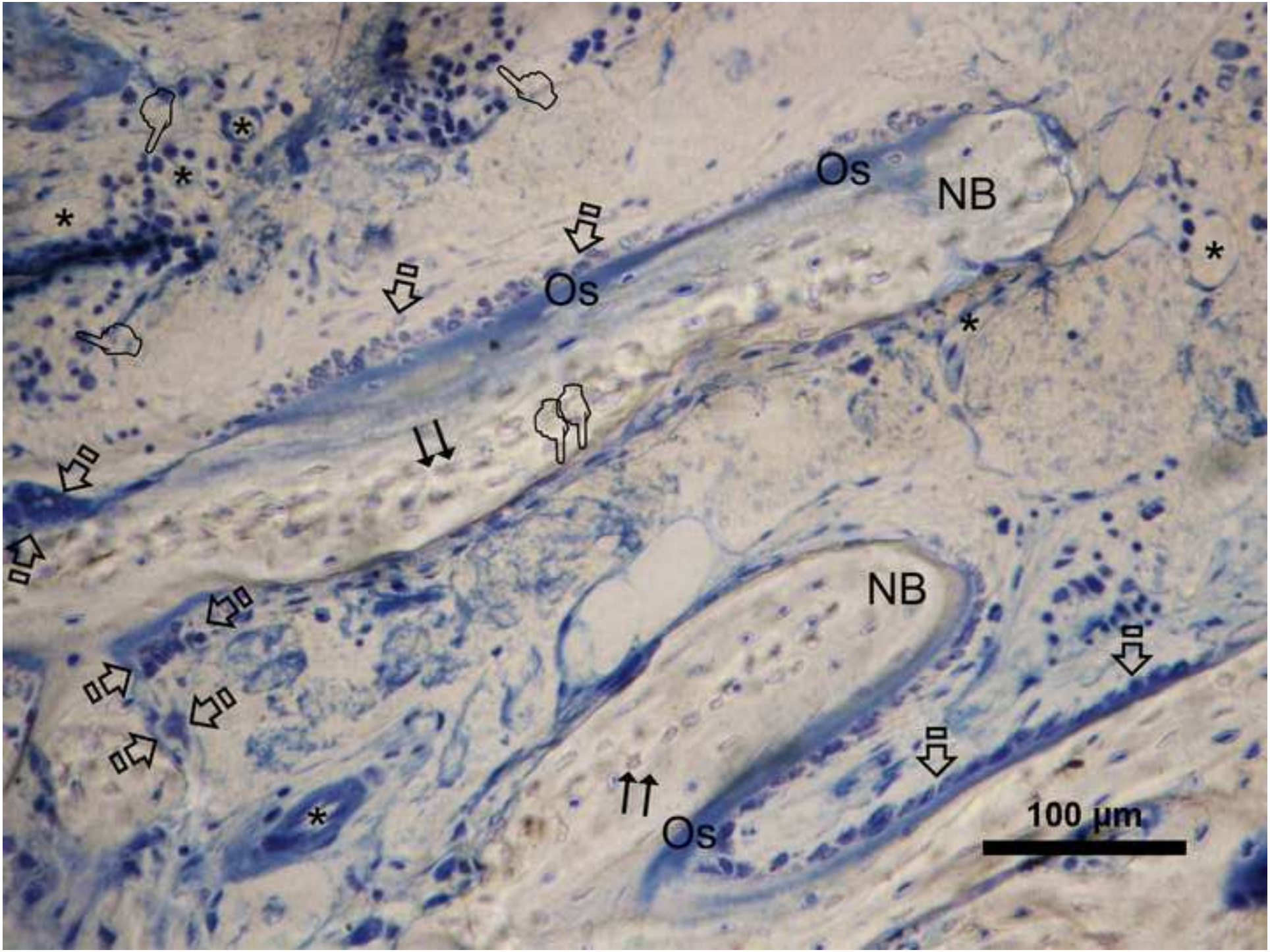

Figure 5

Click here to access/download;Figure;Figure 5.tif

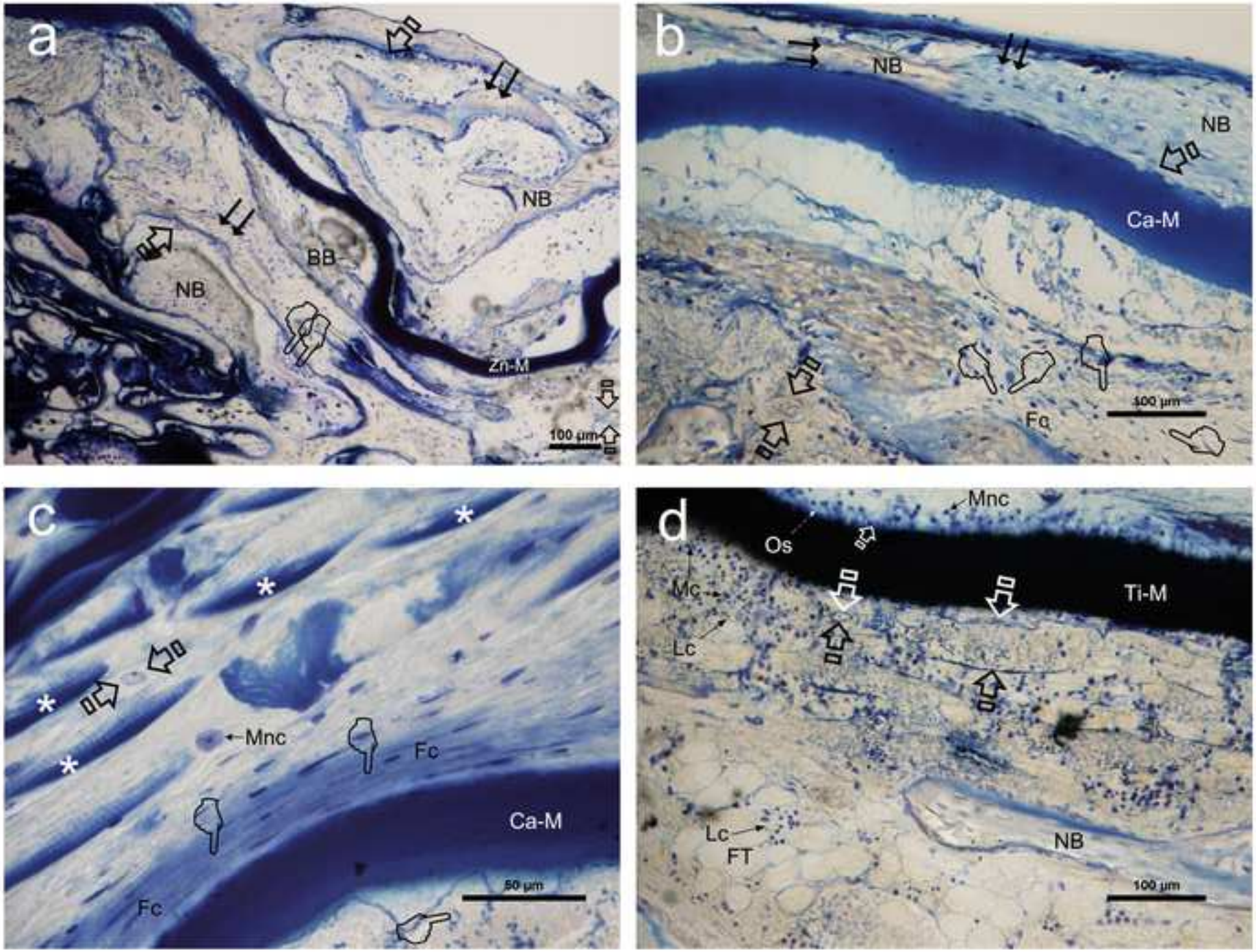

Figure 6

Click here to access/download;Figure;Figure 6.tif

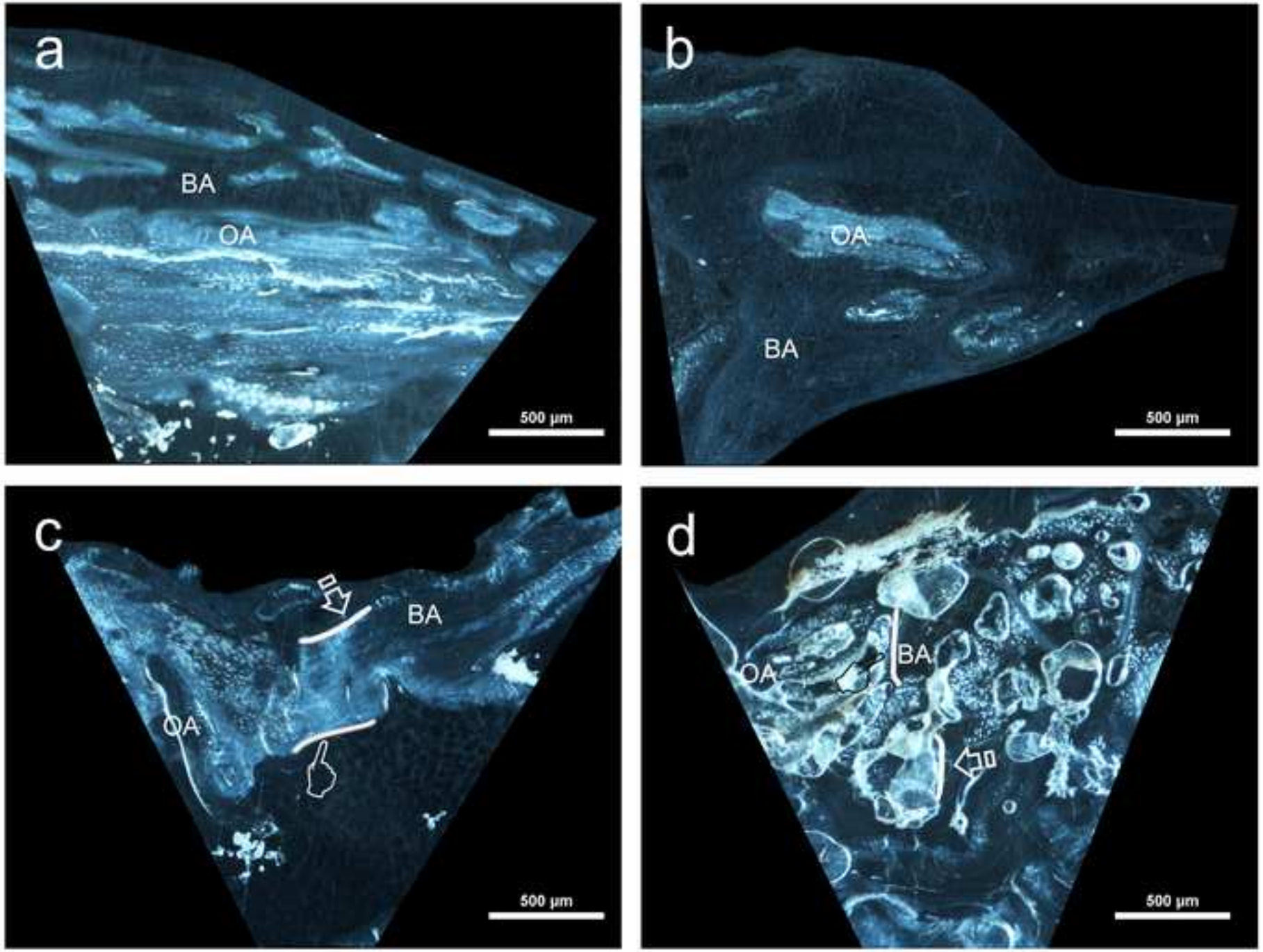

Table 1

Table 1A: Histomorphometric data obtained within the new bone formed at the region of interest (Mean±SD).

	BS (mm^2)	BS/TS (%)	OS (mm^2)	OS/TS (%)	BPm (mm)	BTh (mm)
Ctr	1.63 ± 0.78	0.28 ± 0.07	0.31 ± 0.30	0.05 ± 0.05	46.09 ± 19.86	0.58 ± 0.22
Zn	3.27 ± 1.15	0.39 ± 0.11	0.48 ± 0.24	0.06 ± 0.02	100.33 ± 18.60	1.64 ± 0.23
Ca	2.70 ± 0.82	0.31 ± 0.07	0.46 ± 0.21	0.05 ± 0.02	82.56 ± 37.69	1.58 ± 0.47
BMP	2.47 ± 0.91	0.28 ± 0.07	0.46 ± 0.30	0.05 ± 0.03	79.31 ± 16.32	1.38 ± 0.24
Ti	2.45 ± 0.66	0.31 ± 0.09	0.44 ± 0.14	0.06 ± 0.03	65.15 ± 18.28	1.28 ± 0.31
Unloaded	2.52 ± 0.67	0.29 ± 0.06	0.46 ± 0.20	0.06 ± 0.03	70.37 ± 7.39	1.14 ± 0.37

Table 1B: Statistical results (*P* values). Bold numbers indicate significance at $P < 0.05$.

	BS	BS/TS	OS	OS/TS	BPm	BTh
Ctr - Zn	**0.04**	**0.04**	**0.03**	0.90	0.41	**0.000**
Ctr - Ca	**0.04**	0.17	0.27	0.80	0.31	**0.007**
Ctr - BMP	**0.01**	0.18	0.45	1.00	0.94	**0.006**
Ctr -Ti	**0.03**	0.7	0.11	0.73	0.76	**0.01**
Ctr - Unloaded	**0.03**	0.23	0.18	0.63	0.37	**0.02**
Zn - Ca	0.27	**0.03**	0.86	0.83	0.12	0.83
Zn- BMP	0.16	**0.07**	0.61	0.93	0.50	0.09
Zn - Ti	0.86	**0.01**	0.51	1.00	**0.01**	0.07
Zn - Unloaded	0.23	**0.04**	0.79	0.87	**0.03**	**0.01**

Abbreviations: BS: Bone Surface; OS: Osteoid Surface; BPm: Bone Perimeter; BTh: Bone Thickness; Ctr: control; Zn: zinc; Ca: calcium; BMP: Bone morphogenetic protein; Ti: titanium.

Table 2

Table 2A: Bone cells and blood vessels detected within the new bone formed at the region of interest (Mean±SD).

	Osteocytes/mm^2	**Osteoblasts/mm^2**	**Blood Vessels/mm^2**
Ctr	2934.74 ± 1231.68	154.97 ± 51.66	11.66 ± 2.95
Zn	3359.91 ± 783.15	312.63 ± 92.41	14.77 ± 1.88
Ca	3200.29 ± 1450.04	307.16 ± 96.23	16.31 ± 3.67
BMP	3888.35 ± 1739.98	314.26 ± 164.03	16.35 ± 4.49
Ti	3053.13 ± 924.84	264.76 ± 81.70	6.04 ± 2.62
Unloaded	2796.25 ± 646.30	247.61 ± 66.36	16.58 ± 10.11

Table 2B: Statistical results (*P* values). Bold numbers indicate significance at $P < 0.05$.

	Osteocytes	Osteoblasts	Blood vessels
Ctr - Zn	0.33	**0.00**	0.28
Ctr - Ca	0.45	**0.02**	**0.03**
Ctr - BMP	0.22	**0.04**	**0.04**
Ctr -Ti	0.55	**0.01**	**0.01**
Ctr - Unloaded	0.61	0.11	0.36
Ti- Ca	0.29	0.36	**0.00**
Ti- Zn	0.52	0.15	**0.00**
Ti- BMP	0.18	0.97	**0.00**
Ti- COOH	0.66	0.59	**0.01**
Zn- Ca	0.78	0.38	0.17
Zn- BMP	0.44	0.15	0.47
Zn- Ti	0.52	**0.03**	**0.00**
Zn-Unloaded	0.24	**0.02**	1.00

Abbreviations: Ctr: control; Zn: zinc; Ca: calcium; BMP: Bone morphogenetic protein; Ti: titanium.

Table 3

Table 3A: Histomorphometric data obtained by fluorescence with calcein, within the new bone formed at the region of interest (Mean±SD).

	OA (mm^2)	OA/TS (%)	OP (mm)	BA (mm^2)	BA/TS (%)	BP (mm)
Ctr	0.931 ± 0.593	0.405 ± 0.178	57.868 ± 28.779	1.249 ± 0.514	0.595 ± 0.178	60.716 ± 28.283
Zn	1.018 ± 0.608	0.388 ± 0.223	58.453 ± 29.389	1.589 ± 0.753	0.612 ± 0.223	61.893 ± 28.266
Ca	1.060 ± 0.460	0.426 ± 0.195	70.403 ± 26.119	1.555 ± 0.713	0.574 ± 0.195	72.668 ± 25.001
BMP	1.090 ± 0.557	0.418 ± 0.212	71.024 ± 42.264	1.628 ± 0.779	0.582 ± 0.212	72.909 ± 41.767
Ti	1.088 ± 0.751	0.387 ± 0.221	71.544 ± 39.316	1.588 ± 0.719	0.613 ± 0.221	71.069 ± 37.586
Unloaded	1.159 ± 0.897	0.398 ± 0.271	60.472 ± 24.351	1.682 ± 0.797	0.602 ± 0.271	62.489 ± 25.857

Table 3B: Statistical results (*P* values). Bold numbers indicate significance at $p<0.05$.

	OP (mm)	BA (mm^2)	BP (mm)
Ctr-Unloaded	0.50	**0.01**	0.52
Ca-Zn	**0.03**	0.86	**0.03**

Abbreviations: TS: Total Surface; OA: Osteoid Area; OP: Osteoid Perimeter; BA: Bone Area; BP: Bone Perimeter; Ctr: control; Zn: zinc; Ca: calcium; BMP: Bone morphogenetic protein; Ti: titanium.

Article title: Novel non-resorbable polymeric-nanostructured scaffolds for guided bone regeneration.

Journal Name: Clinical Oral Investigations

Authors: Manuel Toledano[1], José L Gutierrez-Pérez[2], Aida Gutierrez-Corrales[2], María A Serrera-Figallo[2], Manuel Toledano-Osorio[1], Juan I Rosales-Leal[1], Mariano Aguilar[3], Raquel Osorio[1*], Daniel Torres-Lagares[2].

Affiliation and adresses:
1. Dental School. University of Granada. Colegio Máximo, Campus de Cartuja s/n. 18017 Granada, Spain. Research Institute IBS.

2. University of Sevilla, Faculty of Dentistry, Oral Surgery Section. Avicena s/n. 41009 Sevilla. Spain.

3. University of Granada, Faculty of Medicine, Biopathology and Medicine Regenerative Institute (IBIMER, CIBM). Avda. de la Investigación 11. 18016 Granada. Spain.

***Corresponding author:**
Prof. Raquel Osorio.
Email: rosorio@ugr.es

Figure 1 SI

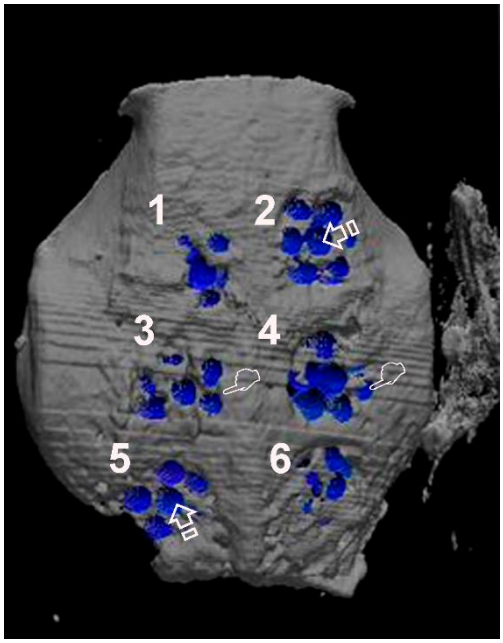

Fig. 1 SI 3D μ-CT image of calvarial defects. Defects treated with unloaded (1), Ti-loaded (2), Zn-loaded (3), Ca-loaded (4), BMP-loaded (5) membranes and an empty control group (6) are observed at one of the rabbit skulls. Threshold at the whole defect (crop) is represented by pointers, and threshold at the centre of the defect (crop 150) is represented by arrows

Table 1A SI: Data from the Micro-CT: *P* values from comparisons performed for variables at the whole defect (crop), after bone trabecular analysis using *PMOD V4.3 FIJI* and *Bone J plus*. Numbers in bold indicate significance at P < 0.05.

	Isosurface	**Skeleton Analysis**					
	BS	Branch	JJVV	SV	Triple P	Max	Sum
Ctr - Zn	**0.01**	**0.04**	**0.04**	**0.03**	**0.03**	0.36	**0.04**
Zn - BMP	0.62	0.07	0.07	0.22	**0.08**	0.81	0.07
Unloaded - BMP	0.55	0.86	0.97	0.80	0.82	**0.02**	0.92

Abbreviations: BS: Bone Surface; Zn: zinc; BMP: Bone morphogenetic protein; JJVV: number of junction voxels; SV: slab voxels; Triple P: triple points; Max: maximum branch length; Sum: total branch length or sum of all branch lengths.

Table 1B SI: Data from the Micro-CT: *P* values from comparisons performed for variables at the centre of the defect (crop 150), after bone trabecular analysis using *PMOD V4.3 FIJI* and *Bone J plus*. Numbers in bold indicate significance at P < 0.05.

	Euler and Connectivity				**Skeleton Analysis**								
	Euler CA	**Vardes**	**Connect**	**connd**	**Branch**	**JJ**	**End-points**	**Juncvo**	**Slabv**	**Triple P**	**Quadr P**	**Max**	**Sum**
Ctr - Zn	**0.04**	**0.04**	**0.04**	**0.04**	**0.03**	**0.03**	**0.03**	**0.03**	**0.02**	**0.03**	0.06	0.36	**0.03**
Ctr - BMP	**0.06**	**0.04**	**0.04**	0.06	0.07	0.06	0.23	0.06	0.19	0.08	0.11	0.17	0.04
Zn - BMP	0.43	0.34	0.34	0.34	0.31	0.35	0.04	0.35	0.39	0.37	0.44	0.36	0.38
Zn-Ca	0.99	0.96	0.96	0.96	0.82	0.76	0.69	0.94	0.52	0.55	0.83	0.04	0.69

Abbreviations: BS: Bone Surface; Zn: zinc; Ca: calcium; BMP: Bone morphogenetic protein; connect: connectivity; Branch: branches; JJ: junctions; Juncvo: junction voxes; Slabx: slab voxes; Triple P: triple points; Quadru P: quadruple points; Max: maximum branch length; Sum: total branch length or sum of all branch length.